In situ structure of the flagellar export apparatus reveals membrane remodeling and lipid-mediated coupling between FlhA and the export gate

Jian Yue[1,2,#,*], Akarsh Manne[3,#], Wangbiao Guo[1,2,#] , Huaxin Yu[1,2], Jiaqi Wang[1,2], Md Khalesur Rahman[3], Kathryn Lees[3], Hui Xu[3], Jack M. Botting[1,2], Md A. Motaleb[3,*] and Jun Liu[1,2,4,5,*]

[1]*Department of Microbial Pathogenesis, Yale School of Medicine, New Haven, CT 06516, USA*
[2]*Microbial Sciences Institute, Yale University, West Haven, CT 06536, USA*
[3]*Department of Microbiology and Immunology, Brody School of Medicine, East Carolina University, Greenville, NC 27834, USA*
[4]*Department of Cell Biology, Yale School of Medicine, New Haven, CT 06510, USA*
[5]*Department of Molecular Biophysics and Biochemistry, Yale University, New Haven, CT 06511, USA*

*** Corresponding authors**:
Jian Yue (**Email**: jian.yue@yale.edu), Md A. Motaleb (**Email**: MOTALEBM@ecu.edu) & Jun Liu (**Email**: jliu@yale.edu)

[#]J.Y., A.M. and W.G. contributed equally.

Supplemental Information

Supplementary Fig. 1	p2
Supplementary Fig. 2	p3,p4
Supplementary Fig. 3	p5
Supplementary Fig. 4	p6
Supplementary Fig. 5	p7,p8
Supplementary Fig. 6	p8
Supplementary Fig. 7	p9,p10
Supplementary Fig. 8	p11
Supplementary Fig. 9	p12,p13
Supplementary Fig. 10	p13
Supplementary Table 1	p14
Supplementary Table 2	p15
Supplementary Table 3	p16,p17

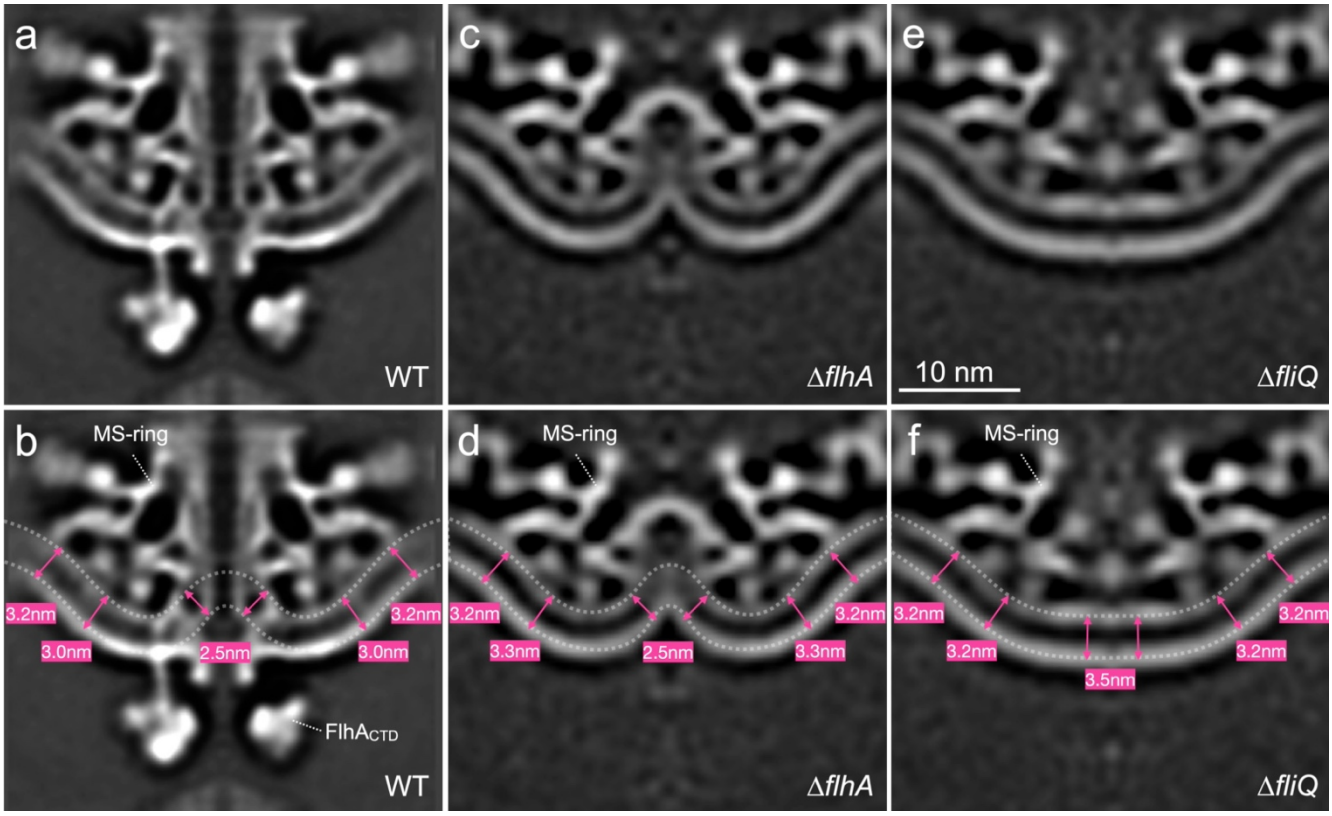

Supplementary Fig. 1 | Membrane leaflet spacing beneath flagellar basal bodies in *B. burgdorferi*. Central section (a) and spacing (b) between the two cytoplasmic membrane leaflets in the wild-type basal body, revealing variable spacing and membrane thinning near the export apparatus. (c, d) Corresponding views for the Δ*flhA* basal body. (e, f) Corresponding views for the Δ*fliQ* basal body.

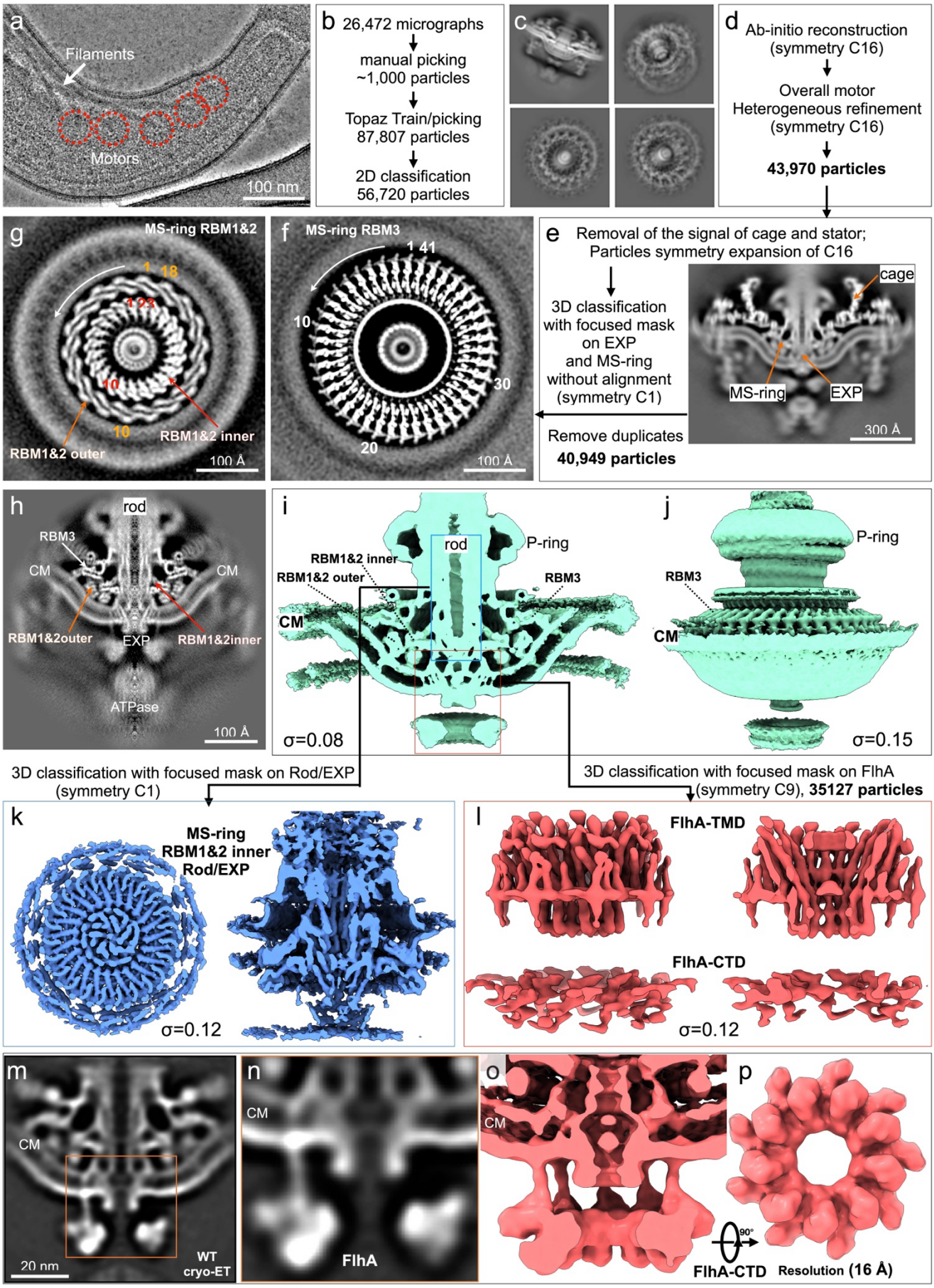
a
Filaments
Motors
100 nm
b 26,472 micrographs
manual picking
~1,000 particles
Topaz Train/picking
87,807 particles
2D classification
56,720 particles
c
d Ab-initio reconstruction
(symmetry C16)
Overall motor
Heterogeneous refinement
(symmetry C16)
43,970 particles
g MS-ring RBM1&2
1 18
1 23
10
10
RBM1&2 outer
RBM1&2 inner
100 Å
f MS-ring RBM3
1 41
10
30
20
100 Å
e Removal of the signal of cage and stator;
Particles symmetry expansion of C16
3D classification
with focused mask
on EXP
and MS-ring
without alignment
(symmetry C1)
Remove duplicates
40,949 particles
cage
MS-ring
EXP
300 Å
h rod
RBM3
CM
CM
RBM1&2outer
EXP
RBM1&2inner
ATPase
100 Å
i rod
P-ring
RBM1&2 inner
RBM1&2 outer
RBM3
CM
σ=0.08
j P-ring
RBM3
CM
σ=0.15
3D classification with focused mask on Rod/EXP
(symmetry C1)
3D classification with focused mask on FlhA
(symmetry C9), 35127 particles
k
MS-ring
RBM1&2 inner
Rod/EXP
σ=0.12
l
FlhA-TMD
FlhA-CTD
σ=0.12
m
CM
20 nm
WT
cryo-ET
n
CM
FlhA
o
CM
p
90°
FlhA-CTD
Resolution (16 Å)

Supplementary Fig. 2 | Overall image processing and structure determination by *in situ* single-particle cryo-EM. (a) Representative micrograph of a *B. burgdorferi* cell tip, with flagellar motors indicated. (b) Particle-picking workflow. From 26,472 micrographs, ~1,000 manually picked particles were used to train Topaz. Iterative picking and classification yielded 56,720 particles. (c) Representative 2D class averages. (d) 3D reconstruction workflow. Ab initio reconstruction (CryoSPARC, C16 symmetry), followed by heterogeneous refinement, yielded 43,970 particles for the overall structure (e). In parallel, removal of collar and stator densities, symmetry expansion (C16), and focused classification (C1, with alignment free) enabled analysis of the export apparatus (EXP) and MS ring (e, left). (f–h) Selected classes revealing MS-ring symmetries: C41 (RBM3), C23 (RBM1–RBM2 inner ring), and C18 (outer ring). (i, j) Surface-rendered MS-ring maps. (k) Focused classification on the central rod (alignment free), yielding classes with clear secondary-structure features. (l) Focused classification on FlhA (alignment free), followed by local refinement and local CTF refinement. (m–p) *In situ* map of the FlhA cytoplasmic domain (CTD) (16 Å resolution) resolved by cryo-ET.

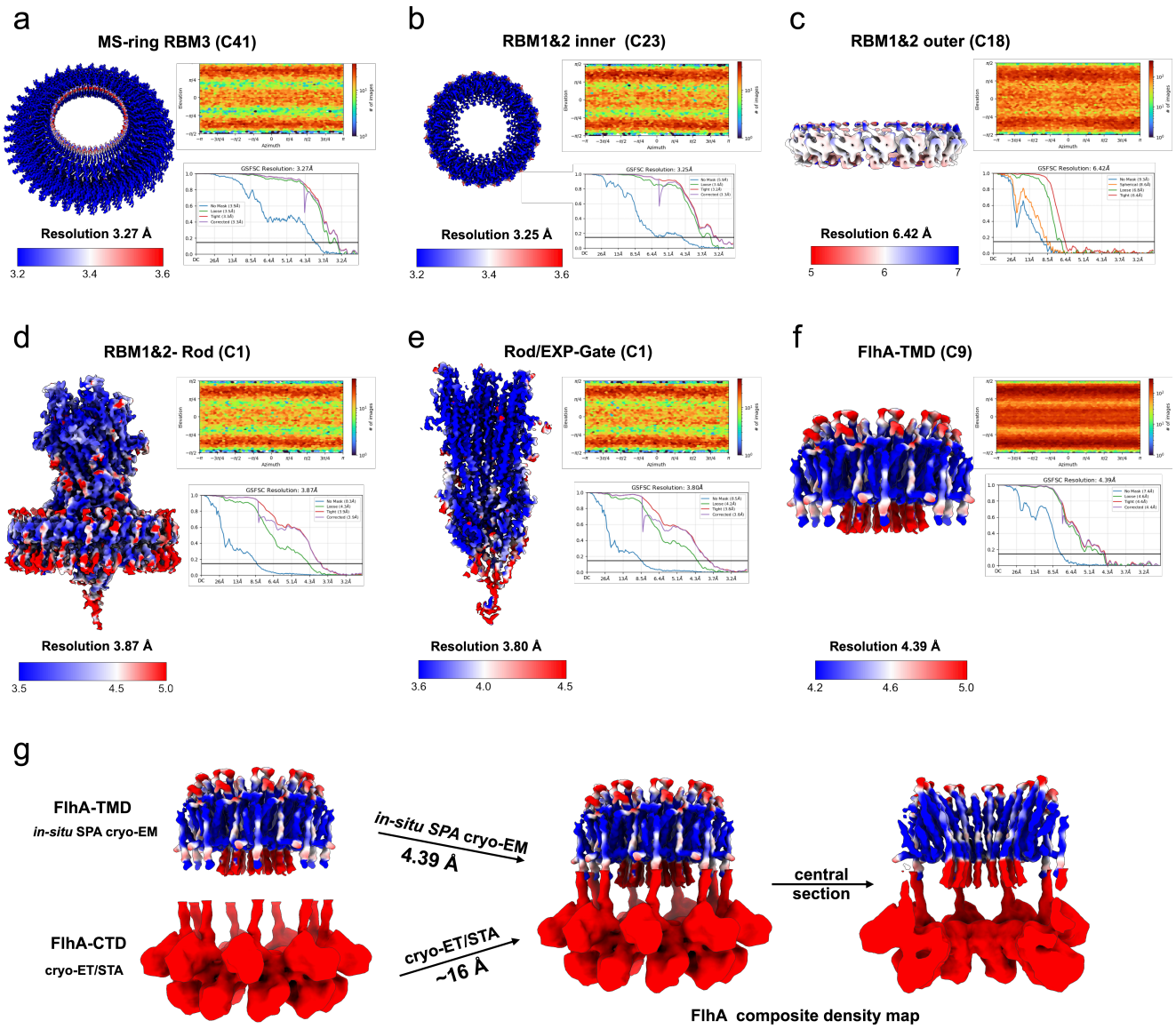

Supplementary Fig. 3 | Resolution estimation and orientation distribution of individual subcomplex maps. (a–c) MS-ring subcomplexes: RBM3 (C41 symmetry), RBM1–RBM2 inner ring (C23 symmetry), and RBM1–RBM2 outer ring (C18 symmetry). (d, e) Export gate–rod assemblies (C1 symmetry). (f) FlhA transmembrane domain (TMD; C9 symmetry). (g) Composite FlhA density map generated by combining the *in situ* single-particle cryo-EM map of $FlhA_{TMD}$ at 4.39 Å with the cryo-ET/subtomogram-averaging reconstruction of $FlhA_{CTD}$ at ~16 Å.

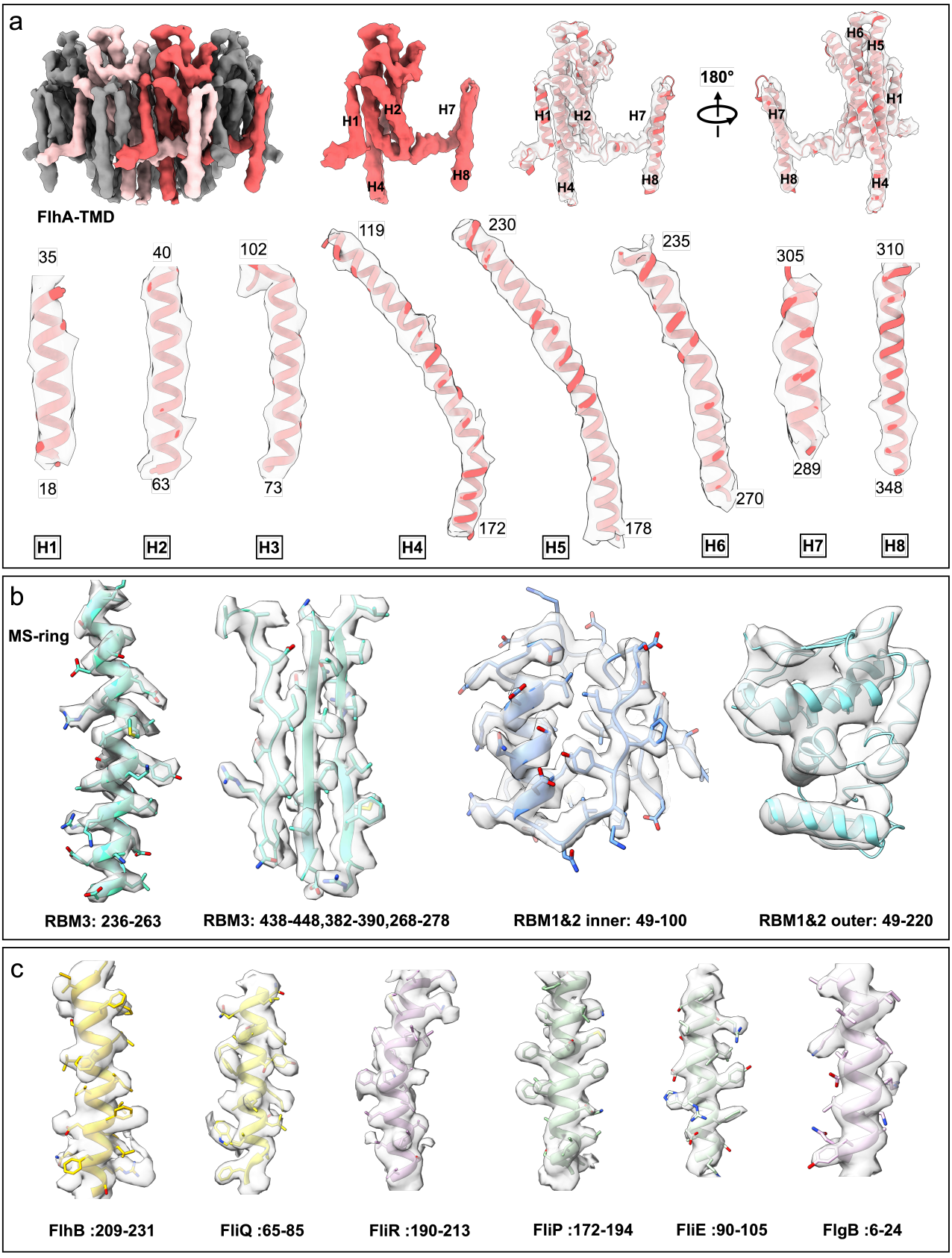

Supplementary Fig. 4 | Representative model-to-map fitting. (a–c) Representative models to map fitting for the $FlhA_{TMD}$ (a), the MS-ring (b), and the FlhB–FliPQR–proximal rod assembly (c).

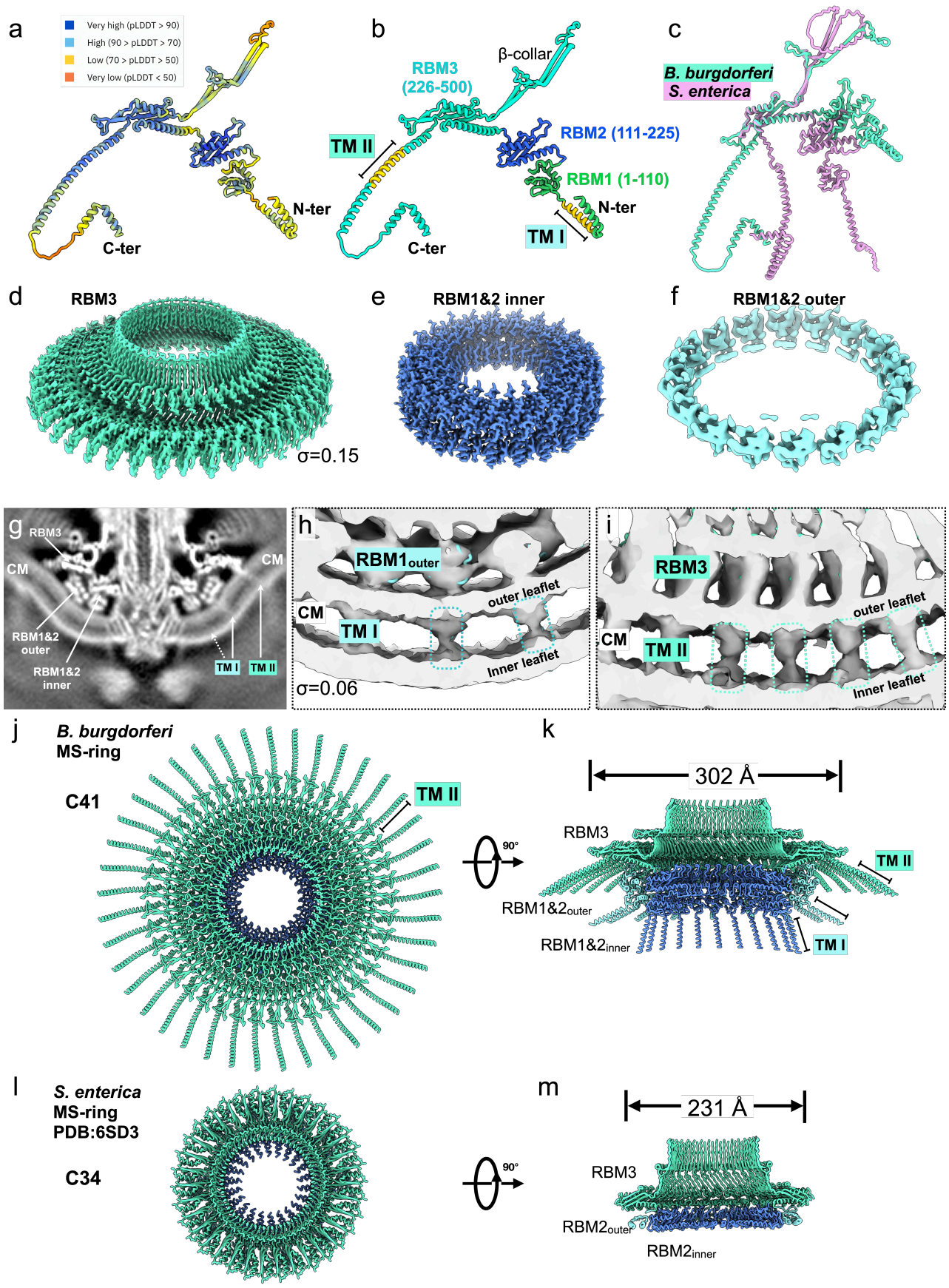
a
Very high (pLDDT > 90)
High (90 > pLDDT > 70)
Low (70 > pLDDT > 50)
Very low (pLDDT < 50)
N-ter
C-ter
b
β-collar
RBM3 (226-500)
TM II
RBM2 (111-225)
RBM1 (1-110)
N-ter
TM I
C-ter
c
B. burgdorferi
S. enterica
d
RBM3
σ=0.15
e
RBM1&2 inner
f
RBM1&2 outer
g
RBM3
CM
CM
RBM1&2 outer
RBM1&2 inner
TM I
TM II
h
RBM1outer
outer leaflet
CM
TM I
Inner leaflet
σ=0.06
i
RBM3
outer leaflet
CM
TM II
Inner leaflet
j
B. burgdorferi
MS-ring
C41
TM II
k
302 Å
90°
RBM3
TM II
RBM1&2outer
RBM1&2inner
TM I
l
S. enterica
MS-ring
PDB:6SD3
C34
m
231 Å
90°
RBM3
RBM2outer
RBM2inner

Supplementary Fig. 5 |Structure of the MS ring. (a) AlphaFold3-predicted structure of a *Borrelia burgdorferi* FliF protomer. (b) Domain organization of FliF. (c) Structural comparison of FliF protomers from *B. burgdorferi* and *S. enterica*, showing conservation at the monomer level. (d–f) Density maps of the individual MS-ring subcomplexes, including the $FliF_{RBM3}$ ring, the inner $FliF_{RBM1–RBM2}$ ring, and the outer $FliF_{RBM1–RBM2}$ ring. (g–i) Model-to-map fitting of densities corresponding to the FliF TMI and TMII helices. (j–m) Comparative analysis of the MS ring from *B. burgdorferi* and *S. enterica* MS ring (PDB 6SD3). Differences in stoichiometry and size, C41 in *B. burgdorferi* versus C34 in *S. enterica*, result in distinct ring dimensions. Densities corresponding to RBM1 and the transmembrane helices are not resolved in the *S. enterica* structure.

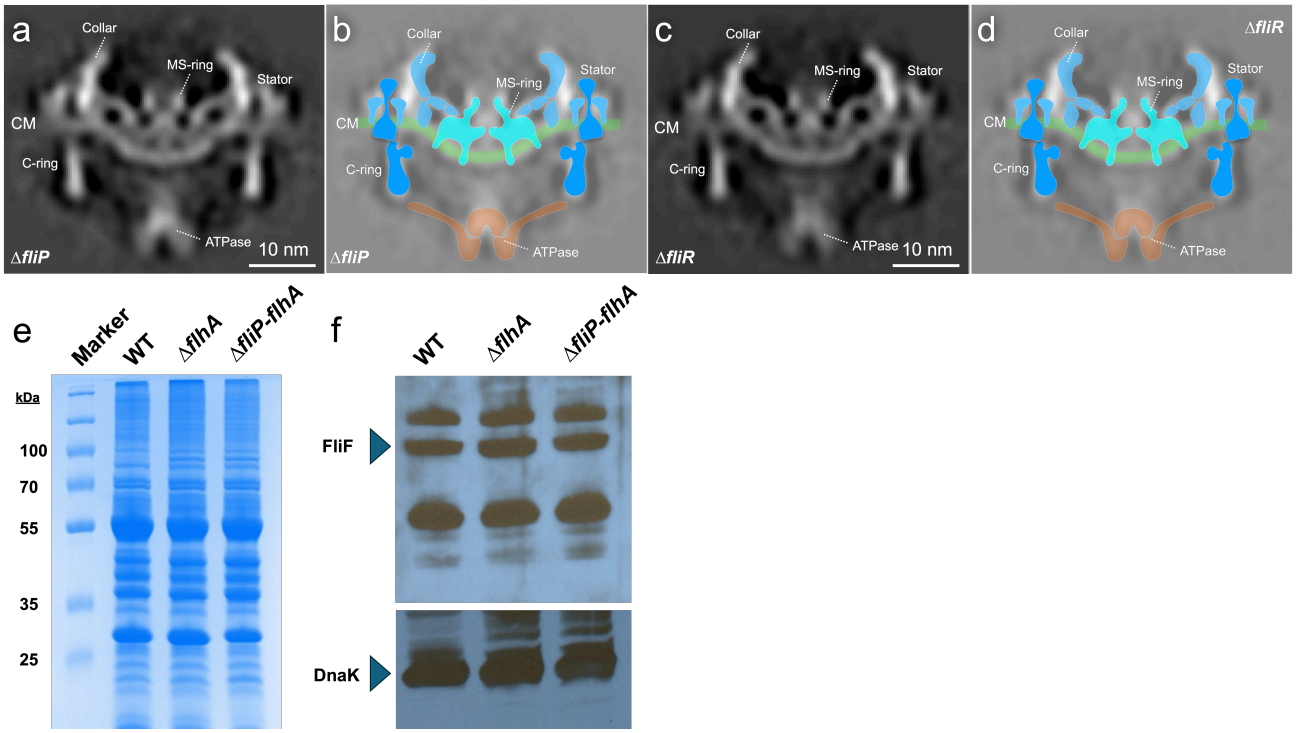

Supplementary Fig. 6 | Characterization of the export apparatus in Δ*fliP* and Δ*fliR* mutants and analysis of FliF expression in the Δ*fliPQR–flhB–flhA* mutant. (a, b) Central section (a) and corresponding schematic model (b) of the basal body structure in the Δ*fliP* mutant, showing absence of FlhA density. (c, d) Central section (c) and corresponding schematic model (d) of the basal body structure in the Δ*fliR* mutant. As in Δ*fliP*, FlhA density is absent, indicating that both FliP and FliR are required for recruitment or stabilization of FlhA. (e, f) Expression amounts of *B. burgdorferi* cell lysates were analyzed by Coomassie blue staining or immunoblotting. Bands corresponding to FliF (65 kDa) and the loading control DnaK (72 kDa) are indicated.

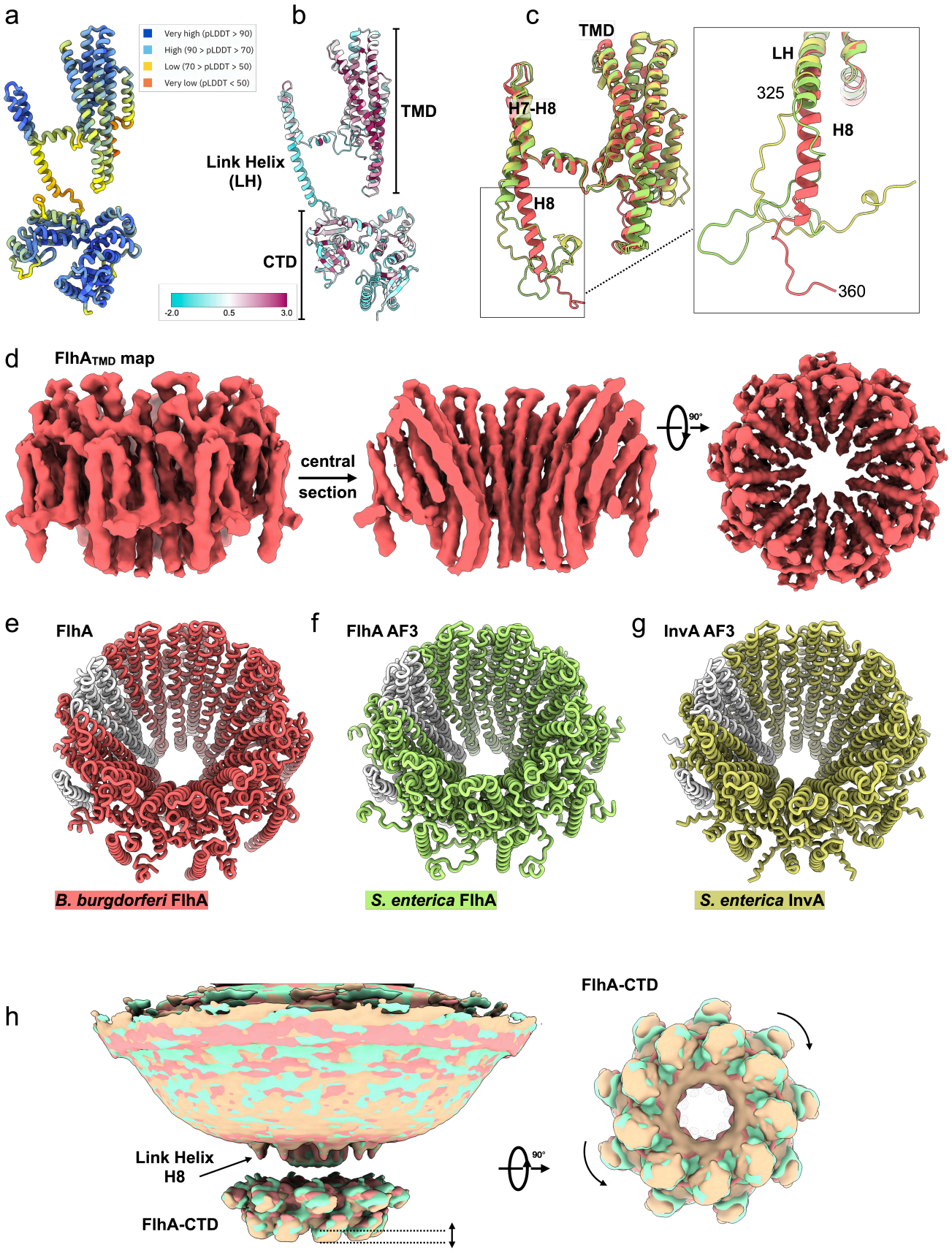
a
Very high (pLDDT > 90)
High (90 > pLDDT > 70)
Low (70 > pLDDT > 50)
Very low (pLDDT < 50)
b
TMD
Link Helix (LH)
CTD
-2.0
0.5
3.0
c
TMD
H7-H8
H8
LH
325
H8
360
d
FlhA$_{TMD}$ map
central section
90°
e
FlhA
B. burgdorferi FlhA
f
FlhA AF3
S. enterica FlhA
g
InvA AF3
S. enterica InvA
h
Link Helix H8
FlhA-CTD
90°
FlhA-CTD

Supplementary Fig. 7 | FlhA structures. (a) AlphaFold-predicted structure of the *B. burgdorferi* FlhA monomer. (b) Domain organization of FlhA, colored by sequence conservation. (c) Structural comparison of FlhA from *B. burgdorferi* and *S. enterica*, and InvA from the *S. enterica* injectisome. The transmembrane domain (TMD) is highly conserved, whereas the linker helix varies, adopting either helical or loop conformations. (d) *In situ* cryo-EM map of $FlhA_{TMD}$ of *B. burgdorferi*. (e–g) Comparison of nonameric structure of *B. burgdorferi* FlhA and AlphaFold-predicted *S. enterica* FlhA and InvA. (h) 3D classification reveals conformational dynamics of the $FlhA_{CTD}$ relative to $FlhA_{TMD}$, including vertical displacement and rotational variation, likely due to the flexibility of linker helix.

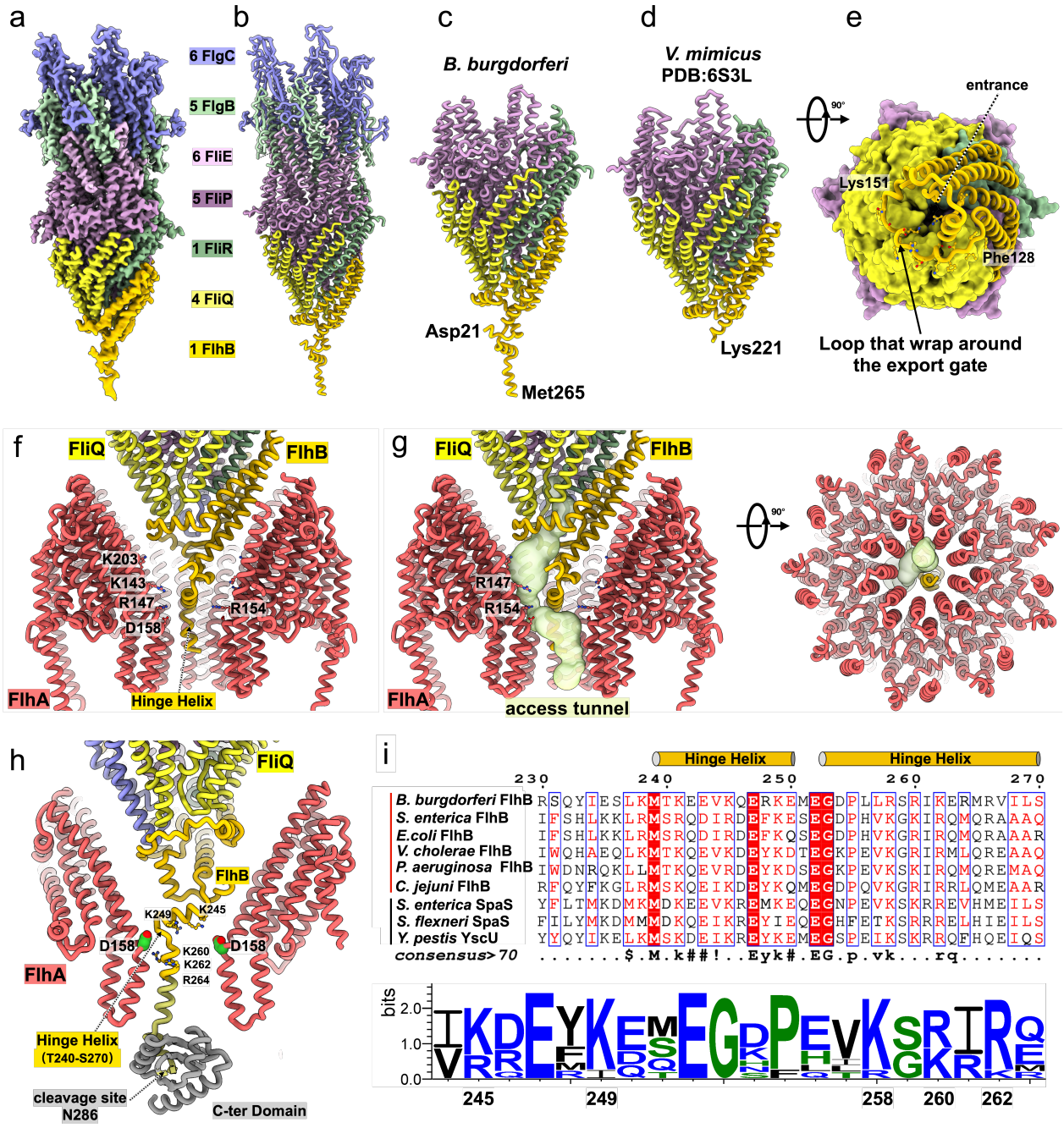

Supplementary Fig. 8 | Spatial organization of the export gate and FlhA. (a) *In situ* cryo-EM map of the export gate and its connected proximal rod, with components and stoichiometries indicated. (b) Structure of the export gate together with the proximal rod. (c, d) Structural comparison of the export gate from *B. burgdorferi* and *V. mimicus* (PDB: 6S3L). Our *B. burgdorferi* structure contains an extended FlhB hinge helix absent from the *V. mimicus* model. (e) Enlarged view of an FlhB loop wrapping around the base of the export gate. (f) Spatial organization of FlhA relative to the FliPQR–FlhB export gate. Conserved basic residues surrounding the substrate entry site are indicated. (g) Access channel calculated using MOLEonline 2.0, illustrating the pathway through the FlhA tunnel to the export gate and its asymmetric orientation. (h) Full-length FlhB model based on the density map and an AlphaFold-predicted structure (grey), showing that the hinge helix is positioned toward one side of FlhA and enriched in basic residues. (i) Sequence alignment of the hinge-helix region highlighting enrichment of conserved lysine and arginine residues.

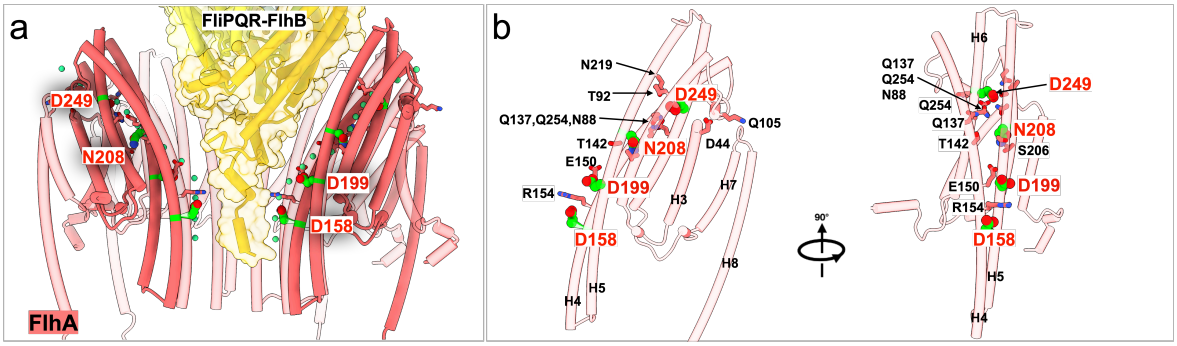
a
FliPQR-FlhB
D249
N208
D199
D158
FlhA
b
N219
T92
D249
Q137,Q254,N88
Q105
T142
N208
D44
E150
R154
D199
H3
H7
D158
H8
H5
H4
90°
H6
Q137
Q254
N88
D249
Q254
Q137
N208
T142
S206
E150
D199
R154
D158
H5
H4

c

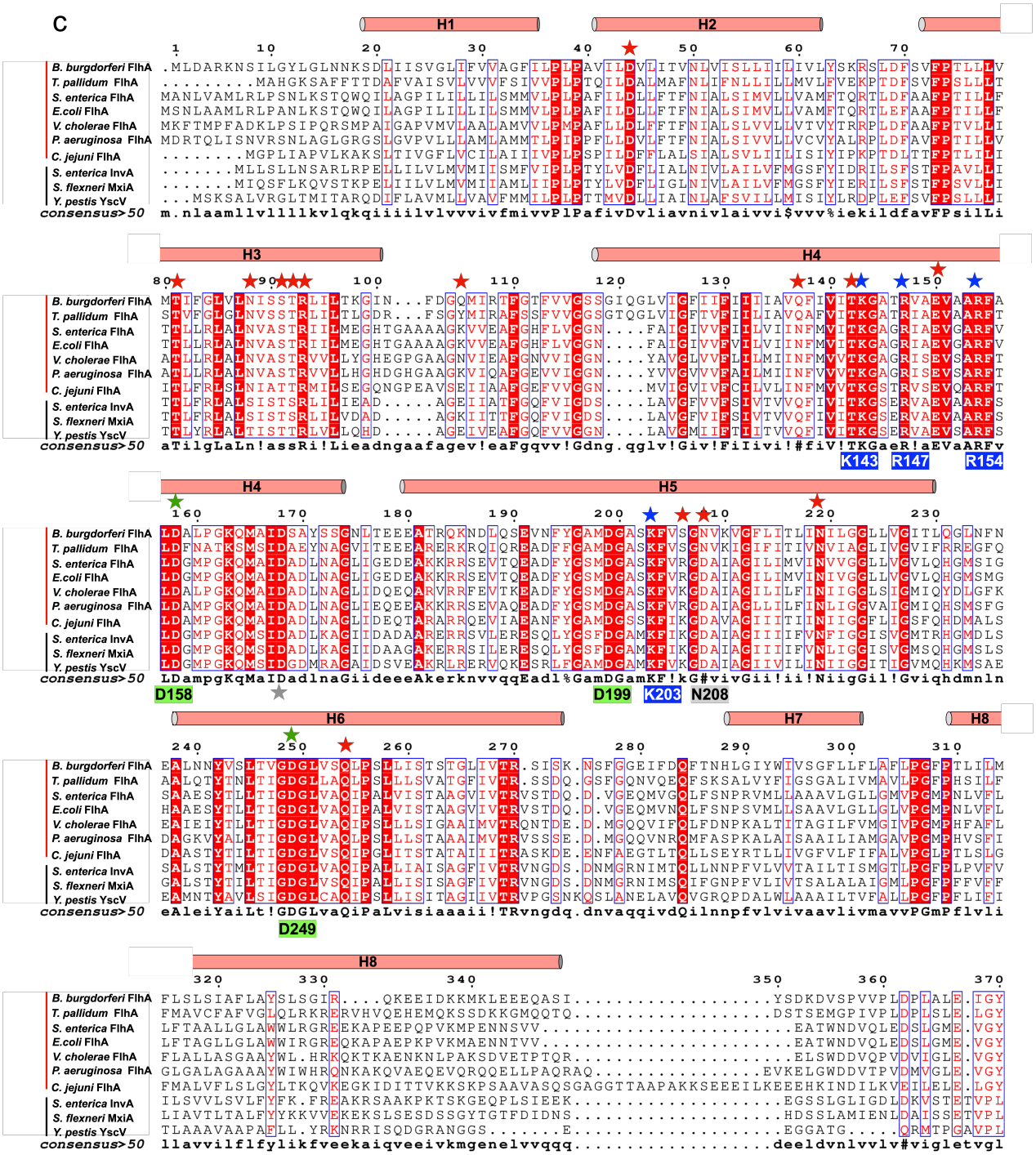
H1
H2
H3
H4
H5
H6
H7
H8
B. burgdorferi FlhA
T. pallidum FlhA
S. enterica FlhA
E.coli FlhA
V. cholerae FlhA
P. aeruginosa FlhA
C. jejuni FlhA
S. enterica InvA
S. flexneri MxiA
Y. pestis YscV
consensus>50
K143
R147
R154
D158
D199
K203
N208
D249

Supplementary Fig. 9 | Hydrophilic pathway of FlhA and its conservation. (a) Hydrophilic pathway within FlhA, with lining residues shown as sticks. Key acidic residues are highlighted (green). (b) Enlarged view of the hydrophilic pathway showing the lining residues. (c) Sequence alignment of FlhA showing conservation. Pathway residues are marked (red stars), with basic (blue) and acidic (green) residues indicated.

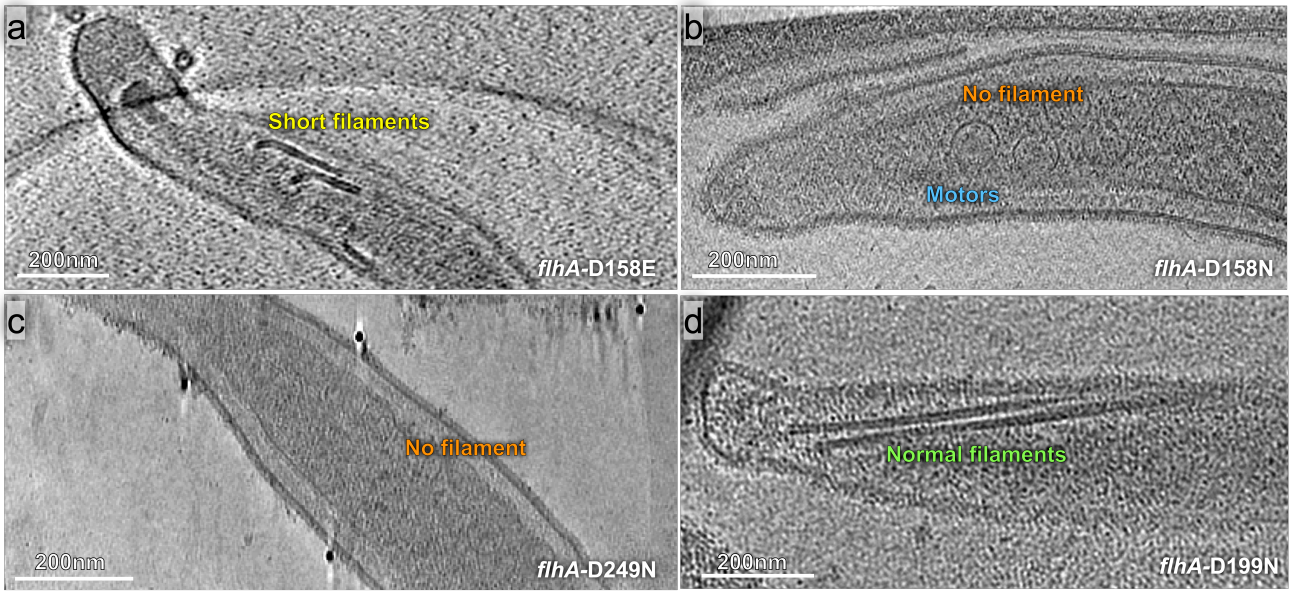

Supplementary Fig. 10 | Representative tomographic slices of FlhA mutants. (a) FlhA-D158E exhibits an abnormally short filament. (b) FlhA-D158N retains an assembled motor but lacks a filament. (c) FlhA-D249N shows an assembled motor without filament. (d) FlhA-D199N shows motor and filament comparable to those of WT.

Supplementary Table 1| Bacterial strains used in this study.

B. burgdorferi	**Gene**	**Gene product**	**Motility**	**Reference**
Wild type	N/A	N/A	motile	Zhao. *et al.* (2013)
Δ*fliP-flhA*	N/A	N/A	nonmotile	This study
Δ*flhA*	bb0271	Flagellar biosynthesis protein FlhA	nonmotile	This study
Δ*flhB*	bb0272	Flagellar biosynthesis protein FlhB	nonmotile	This study
Δ*fliP*	bb0275	Flagellar biosynthesis protein FliP	nonmotile	This study
Δ*fliQ*	bb0274	Flagellar biosynthesis protein FliQ	nonmotile	This study
Δ*fliR*	bb0273	Flagellar biosynthesis protein FliR	nonmotile	This study
flhA-D158N	bb0271	A point mutation in FlhA	nonmotile	This study
flhA-D158E	bb0271	A point mutation in FlhA	less motile	This study
flhA-D199N	bb0271	A point mutation in FlhA	motile	This study
flhA-D249N	bb0271	A point mutation in FlhA	nonmotile	This study

Supplementary Table 2| Cryo-ET data collection and parameters.

Genotype	No. of Tomograms	No. of Motors	Microscope/ Detector	Magnification	Pixel size (Å)	Resolution (Å)	Accession code
Wild type	480	4322	Titan Krios/ Gatan K3	42,000	2.15	15.9	EMD-48080
Δ*fliQ*	735	4042	Titan Krios/ Gatan K3	42,000	2.15	16.0	EMD-48081
Δ*flhA*	429	3479	Titan Krios/ Gatan K3	42,000	2.15	21.0	EMD-48082
flhA-D158N	85	700	Titan Krios/ Gatan K3	42,000	2.15	N/A	N/A
flhA-D158E	126	1009	Titan Krios/ Gatan K3	42,000	2.15	N/A	N/A
flhA-D199N	101	541	Titan Krios/ Gatan K3	42,000	2.15	N/A	N/A
flhA-D249N	68	409	Titan Krios/ Gatan K3	42,000	2.15	N/A	N/A
Δ*fliP-flhA*	342	54	Polara/CCD	31,000	5.7	63.0	EMD-6094
Δ*flhB*	217	534	Polara/CCD	31,000	5.7	58.0	EMD-6089
Δ*fliP*	265	359	Polara/CCD	31,000	5.7	48.0	EMD-6091
Δ*fliR*	229	830	Polara/CCD	31,000	5.7	41.0	EMD-6093

Supplementary Table 3| Data Collection and Structure Refinement Statistics.

	MS-ring (RBM3)	MS-ring (RBM1&2$_{inner}$)	MS-ring (RBM1&2$_{outer}$)	Export gate-rod
Data collection				
Microscope	Titan Krios	Titan Krios	Titan Krios	Titan Krios
Voltage (kV)	300	300	300	300
Camera	K3	K3	K3	K3
Magnification	81K	81K	81K	81K
Total Electron Exposure (e^-/Å^2)	70	70	70	70
Defocus range (um)	-1.5 to -2.2	-1.5 to -2.2	-1.5 to -2.2	-1.5 to -2.2
Pixel size (Å)	1.068	1.068	1.068	1.068
Micrographs (no.)	26,472	26,472	26,472	26,472
Data processing				
Symmetry imposed	C41	C23	C18	C1
Final particle images (No.)	40,949	37,987	37,987	37,987
Map resolution (Å) 0.143 FSC threshold	3.37	3.25	6.42	3.87
Map sharpening B factor (Å^2)	-97.1	-87.7	NA	-39.9
Refinement				
CC (model vs. data)	0.73	0.78	0.79	0.82
Non-hydrogen atoms	86,264	37,536	29052	61,250
Protein residues	10,742	4,807	3,636	7,834
Ligands	0	0	0	0
B factors (Å^2)				
Proteins	110.61	45.31	360.56	108.94
R.m.s. deviations				
Bond lengths (Å)	0.004	0.004	0.002	0.003
Bond angles (°)	0.492	0.580	0.511	0.643
Validation				
MolProbity score	1.97	2.27	1.64	2.02
Clashscore	5.10	6.24	4.32	4.25
Rotamer outliers (%)	3.06	4.91	3.56	3.76
Ramachandran plot				
Favoured (%)	95.32	94.08	93.43	94.45
Allowed (%)	4.68	5.46	6.06	5.41
Outliers (%)	0.00	0.46	0.51	0.14
PDB code	**12DR**	**12DS**	**12DT**	**12DU**
EMDB code	**EMD-76344**	**EMD-76345**	**EMD-76346**	**EMD-76347**

	FlhA-TMD (1-350aa)	Overall EXP and MS-ring
Data collection		
Microscope	Titan Krios	Titan Krios
Voltage (kV)	300	300
Camera	K3	K3
Magnification	81K	81K
Total Electron Exposure (e^-/Å^2)	70	70
Defocus range (um)	-1.5 to -2.2	-1.5 to -2.2
Pixel size (Å)	1.068	1.068

Micrographs (no.)	26,472	26,472
Data processing		
Symmetry imposed	C9	/
Final particle images (No.)	35,127	/
Map resolution (Å) 0.143 FSC threshold	4.39	/
Map sharpening B factor ($Å^2$)	-165.9	/
Refinement		
CC (model vs. data)	0.77	/
Non-hydrogen atoms	24,075	231,030
Protein residues	3,150	29,166
Ligands	0	0
B factors ($Å^2$)		
Proteins	175.44	NA
R.m.s. deviations		
Bond lengths (Å)	0.002	0.002
Bond angles (°)	0.503	0.499
Validation		
MolProbity score	1.80	1.72
Clashscore	5.83	3.59
Rotamer outliers (%)	3.02	3.04
Ramachandran plot		
Favoured (%)	97.41	96.72
Allowed (%)	2.59	3.14
Outliers (%)	0.00	0.14
PDB code	**12DV**	**12DW**
EMDB code	**EMD-76348**	**EMD-76349**